Hybridization of circular and rectangular transverse profiles of nanophotonic modes for nonlinear optics

XIYUAN LU[1,2,*], WEI C. JIANG[3], AND KARTIK SRINIVASAN[1,4,5]

[1] Microsystems and Nanotechnology Division, Physical Measurement Laboratory, National Institute of Standards and Technology, Gaithersburg, MD 20899, USA
[2] Institute for Research in Electronics and Applied Physics and Maryland NanoCenter, University of Maryland, College Park, MD 20742, USA
[3] Science and Technology Division, Corning Research and Development Corporation, Corning, New York 14831, USA
[4] Joint Quantum Institute, NIST/University of Maryland, College Park, MD 20742, USA
[5] e-mail: kartik.srinivasan@nist.gov
[*] Corresponding author: xiyuan.lu@nist.gov

Compiled June 3, 2021

Nanophotonic modes within rectangular cross-sections are typically considered to have transverse rectangular field p rofiles. In th is wo rk, we sh ow th at, despite the rectangular cross-section of most integrated waveguides and microring resonators, there exists considerable hybridization of transverse rectangular modes and transverse circular modes. These hybridized modes can be advantageous in nonlinear wave mixing processes. We use third-harmonic generation as an example to confirm that such hybridized modes have benefits with respect to reasonable mode overlap and waveguide coupling to a fundamental mode in a silicon nitride microring. Our work illuminates the potential of using transverse circular modes in nanophotonic applications.

Optical fibers are a key lightwave technology for building long-distance communication systems [1]. Among various types of fibers, those with a circular core and cladding are used most often. In such fibers, there are typically transverse electric (TE) modes, transverse magnetic (TM) modes, and modes that are a hybrid of TE and TM (HE/EH). In weakly guilding fibers, these optical modes are degenerate and thus designated in the form of linear polarization (LP) modes. Such LP modes, typically labeled as LP_{ij}, are described by two indices, an angular mode number (i = 0, 1, 2, etc.) and a radial mode number (j = 1, 2, 3, etc.); hereafter, we will use the labeling scheme cij to connect these modes to those of the nanophotonic devices we will be considering. A schematic of a step-index optical fiber and nine cij modes are illustrated in Fig. 1(a). In a single mode fiber, only the fundamental mode (LP_{01}, now termed c01) is allowed and all other higher-order modes are cut-off.

While optical fiber with a circular core is the waveguiding component used most in optical communication, it is not suitable for many other functions needed in lightwave technology [2]. In particular, planar waveguides with rectangular cross-section are compatible with photolithography and semiconductor fabrication techniques. These planar waveguides not only can realize various components such as couplers, ring resonators, lasers, and modulators, but also can potentially enable large-scale photonic integration, which offers complex functionalities, miniature footprint, and ultra-low power consumption. While weakly guided planar waveguides can support LP modes with circular symmetry, as has been used for mode-division multiplexing [3, 4], planar waveguides with high-index contrast like silicon-on-insulator (SOI) support modes in which all six components of the electric and magnetic fields have non-zero amplitude. Typically, there is a dominant electric (or magnetic) field component for such modes, which are denoted as quasi-TE (or quasi-TM), abbreviated as TE (or TM) hereafter. Figure 1(b) shows a schematic of such a nanophotonic waveguide, consisting of a rectangular core described by its width and height and with substrate on the bottom and cladding on top, along with the nine TE modes it supports. These TE modes all have a dominant field component E_x with transverse mode profiles labeled by rij, where i and j represent horizontal and vertical anti-nodes, respectively. Nanophotonic waveguides are also widely used in nonlinear optics [5, 6] because of their strong modal confinement, strong geometric control of dispersion, and enhanced nonlinear interaction. Microring resonators provide temporal build-up of the field in addition to the spatial confinement (in nanophotonic waveguides), and further increase the efficiencies in nonlinear optics [7, 8]. In microrings, the TE/TM designation for the transverse mode profiles is used, in correspondence with the waveguide case.

In this work, we raise attention to the hybridization of circular and rectangular transverse mode types in nanophotonics, and how these hybridized modes may play an important role in nonlinear optical processes such as third harmonic generation. We use the silicon nitride (Si_3N_4) nanophotonic platform [7] because it has been established for wide-band nonlinear optics, including microresonator frequency comb generation [7, 8], optical frequency conversion [9, 10], optical parametric oscillation [11], supercontinuum generation [12, 13], and second/third harmonic generation [14–17]. Although in such a rectangular geometry, rectangular modes are mostly considered and used in various applications [7–17], Fig. 1(c) shows the results of finite-element simulations illustrating that, hybridization of rect-

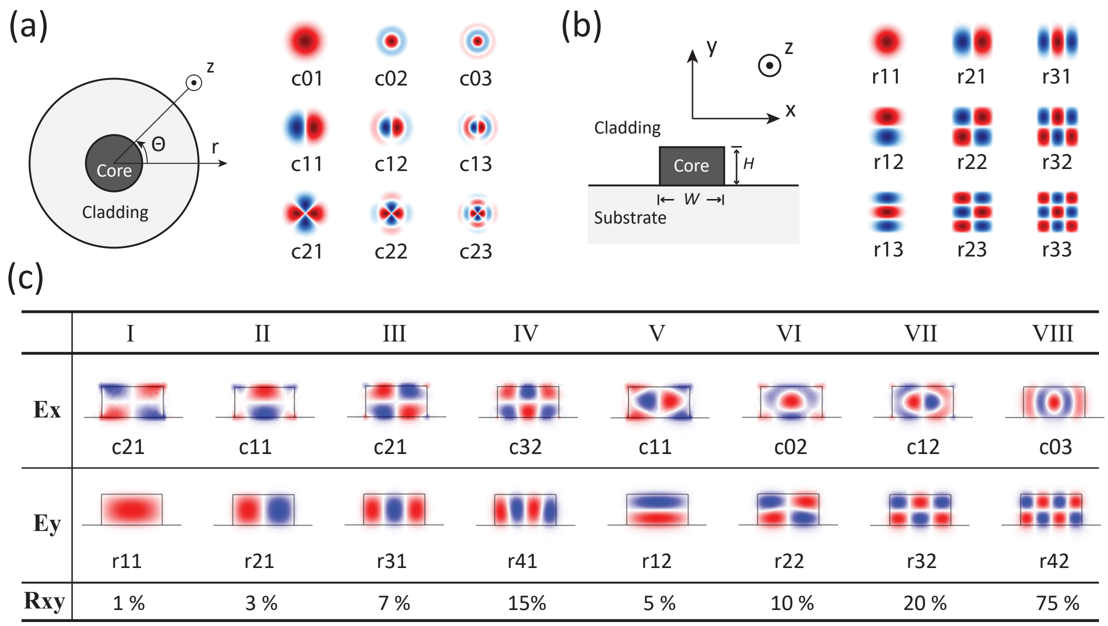

Fig. 1. Typical circular and rectangular transverse mode profiles and their hybridization. (a) Photonic waveguide with a circular cross-section (e.g., optical fiber) shown in polar coordinates (left). Such a waveguide supports transverse circular mode profiles whose electric field amplitudes we qualitatively illustrate (right). We label these modes as cij, where i and j represent angular and radial mode numbers, respectively, with j anti-nodes when $i = 0$ and $2i \times j$ anti-nodes when $i > 0$. **(b)** Nanophotonic waveguide with rectangular cross-section depicted in cartesian coordinates (left), with the core defined by its width (W) and height (H), a cladding on top, and substrate on the bottom. Such a waveguide typically supports transverse rectangular mode profiles, which we qualitatively illustrate (right) and label as rij, where i and j represent horizontal and vertical mode numbers, respectively (right). Following this definition, a rectangular mode rij has $i \times\ j$ anti-nodes. **(c)** Finite-element-method (FEM) simulation results show hybridization of circular and rectangular transverse profiles in a Si_3N_4 nanophotonic rectangular waveguide. The device is simulated at a wavelength of 520 nm in a waveguide with W = 1200 nm and H = 600 nm, with air cladding on top and silicon oxide substrate at bottom. All the displayed modes have E_x with circular transverse profiles (labeled by cij) and E_y with rectangular transverse profiles (labeled by rij). The dominant field component of these modes is E_y, and the ratio of the maximal field strength of E_x and E_y is listed as Rxy = max(E_x)/max(E_y). We note that from an energy distribution perspective, the ratio would be different, but in general can be estimated by Rxy and the number of antinodes in the mode profiles.

angular and circular transverse modes can exist in certain circumstances. We choose Si_3N_4 waveguides with geometries that are commonly used in nonlinear optics [7, 8], which are relatively thick and have much larger aspect ratios (in this case W:H = 1200 nm:600 nm = 2:1) than most waveguides used in linear applications. These larger aspect ratio waveguides are highly multi-moded, particularly at short wavelengths. Besides the large aspect ratio, the low refractive index contrast is also in favor of such mode hybridization. The index contrast here, though stronger than in a weak confinement planar waveguide, is much weaker for Si_3N_4 to SiO_2 ($\approx$ 2.0:1.5) than Si to SiO_2 ($\approx$ 3.5:1.5). Amongst the various modes such a waveguide supports at λ = 520 nm, we display the hybridized modes that have circular profiles in E_x and rectangular profiles in E_y, with their profiles labeled in Fig. 1(c). We find circular modes c02 (VI), c12 (VII), and c03 (VIII) that have no clear counterpart rectangular modes, modes c11 and c21 in two orientations (II/V and I/III, respectively) that are similar to rectangular modes like r12/r21 and r22, but differ in curvature and number of nodes, and mode c32 (IV) that differs from r32 mostly in curvature. We note that c01 is degenerate with r11 and not shown here.

Such hybridized modes have dispersion and coupling properties different than conventional modes, which can be beneficial for nonlinear optical processes including optical parametric oscillation, Kerr frequency combs, and second-/third-harmonic generation. Here, we use third-harmonic generation [13, 14, 16] as an example, as f-3f conversion has the widest frequency separation between pump and output signal allowed by $\chi^{(3)}$ nonlinear optics, and is therefore one of the most challenging nonlinear processes to realize. Circular modes can have advantages in microring-waveguide coupling in comparison to rectangular modes, while offering similar dispersion engineering capabilities. For example, $c0j$ modes can have dispersion engineering similar to that of $r1j$ because of the similarity in vertical confinement, but are in general much easier to couple to the fundamental modes of an access waveguide as the $c0j$ modes have only one anti-node in the vertical direction. In contrast, $r1j$ (j>1) modes have multiple anti-nodes in the vertical direction, making their coupling to fundamental waveguide modes much weaker. Furthermore, these circular modes have advantages in mode overlap compared to rectangular modes. For example, $c0j$ modes (e.g., VI, VIII) can overlap much better with the fundamental rectangular mode (r11) than high-order rij modes can. The aforementioned benefits are only fully realized if the hybridized modes distribute enough energy in the field component exhibiting circular profiles (E_x in this case). To quantify the strength of the hybridization, we calculate Rxy = max(E_x)/max(E_y) for these hybridized modes (Fig. 1(c)). We notice that, for cij modes

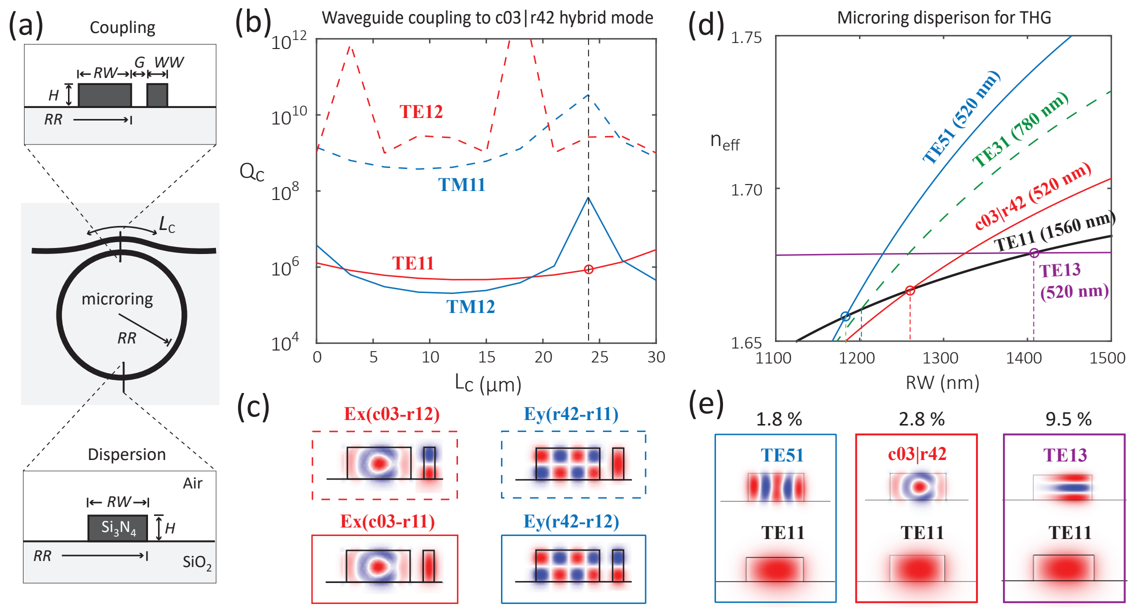

Fig. 2. Hybridized modes in microring nonlinear optics. **(a)** Device schematic showing a Si_3N_4 microring coupled with a pulley waveguide. The top cross-section illustrates the waveguide-microring coupling design and the bottom microring cross-section determines the dispersion design. *RR*: Ring radius. *H*: Height/thickness. *RW*: Ring width. *G*: Coupling gap. *WW*: Waveguide width. L_c: Coupling length. **(b)** Coupling between the c03 | r42 hybridized microring mode (E_x component has a c03 profile and E_y component has a r42 profile) and the first four waveguide modes. These four modes are TE11 (dominant field component is E_x with r11 profile, solid red), TE12 (E_x with r12 profile, dashed red), TM11 (E_y with r11 profile, dashed blue), and TM12 (E_y with r12 profile, solid blue). The coupling quality factor Q_c is calculated for a pulley waveguide with WW = 200 nm and G = 150 nm, and the coupling length L_c is varied. Because of the vertical symmetry (asymmetry) of E_x (E_y) for the hybridized mode, it couples much better to TE11 (TM12) ($Q_c \approx 10^6$) than TE12 (TM11) ($Q_c > 10^9$). L_c =24 μm (dashed black vertical line) is an especially suitable coupling design, in which only the TE11 mode exhibits appreciable coupling ($Q_c \approx 10^6$). **(c)** Illustration of these four coupling paths, where major coupling field components are displayed (E_x for TE12 and TE11, E_y for TM11 and TM12). Dashed (solid) lines outline the coupling paths that have different (same) symmetry in the vertical direction. **(d)** Microring mode effective indices with varying *RW* (*RR* = 23 μm and *H* = 600 nm) for five modes: TE11 (E_x with r11 profile) at the pump wavelength of 1560 nm (black), TE51 (E_x with r51 profile, blue) at 520 nm, c03 | r42 (E_x with c03 profile and E_y with r42 profile, red) at 520 nm, and TE13 (E_x with r13 profile, purple) at 520 nm, and TE31 (E_x with r31 profile, dashed green) at 780 nm. The TE51, c03 | r42, and TE13 modes have phase-matching for THG at *RW* = {1185, 1260, 1410} nm. The TE31 mode has phase matching for SHG at *RW*=1200 nm, and cannot phase match for THG within the simulated parameter range. **(e)** The mode profiles for the THG modes (top) at 520 nm and the pump modes (bottom) at 1560 nm, with the device geometry specified by the circles in (d) with corresponding colors. The mode overlap percentages are specified for each configuration, and the mode volumes are {53.1, 53.0, 51.2} μm^3 for {TE51, c03 | r42, TE13}.

with the same i, modes with higher j seem to be hybridized more, that is, have a larger Rxy. For example, the c03 | r42 mode (VIII) shows Rxy ≈ 75 %.

To validate the usefulness of hybridized modes for nonlinear optics, we use the c03 | r42 mode in a 23-μm-radius Si_3N_4 microring as an example. Previously, we have only considered the hybridized mode in straight waveguides (Fig. 1), but hereafter we consider the hybridized modes in microrings, which are more attractive for low-power nonlinear optics [10]. Although the bending effect perturbs the straight waveguide modes, the fundamental characteristic of the hybridized modes remains the same in microrings (see Supplementary). We first show that the c03 | r42 microring mode can be efficiently coupled to the TE11 mode in a pulley waveguide, that is, a waveguide wrapped around the microring with a constant gap, as shown in Fig. 2(a). While we use TE/TM notation for conventional (non-hybridized) modes of waveguides and microrings, the *rij* notation can be equivalently used, and both labeling schemes are provided in the caption to Fig. 2. The coupling quality factor Q_c, which is inversely proportional to the resonator-waveguide coupling rate, is calculated using a coupled mode theory formalism [9, 18]. Here we consider all other relevant modes in the microring and coupling waveguide, and show the dominant field components that contribute to coupling in Fig. 2(c). The c03 | r42 microring mode can be efficiently coupled to TE11 and TM12 waveguide modes (solid lines), with $Q_c \approx 10^6$ achievable at a gap of 150 nm; lower Q_c is achievable with smaller coupling gaps. The c03 | r42 mode is poorly coupled to TE12 and TM11 (dashed lines, $Q_c > 10^8$), because of the opposite parity of the microring and waveguide field profiles in the vertical direction. Moreover, by tuning the pulley coupling length (L_c) to 24 μm (open circle in Fig. 2(b)), the hybridized mode is coupled only to the TE11 waveguide mode, which is a fundamental mode that can be efficiently extracted to fiber. The TM12 waveguide mode, which has two anti-nodes in Ey, is at an anti-phase-matching point [18] at L_c = 24 μm.

Aside from waveguide coupling, phase matching is crucial for nonlinear optics. We simulate the potential for using the

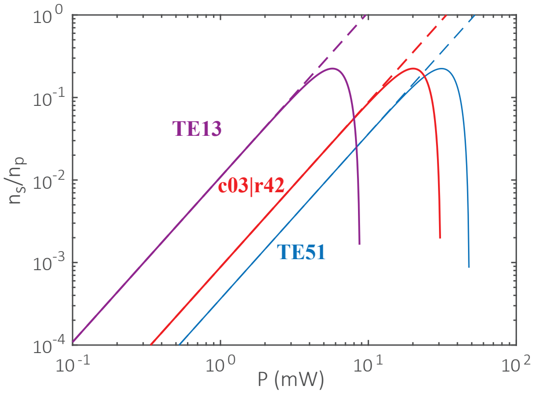

Fig. 3. THG efficiencies. Calculated THG conversion efficiency for the different phase-matched mode options, with (solid lines) or without (dashed lines) pump depletion. The conversion efficiency is the ratio of the waveguide output signal flux (n_s) to the waveguide input pump flux (n_p).

c03 | r42 mode in microcavity third-harmonic generation (THG). To realize phase-matching for THG, in which the modal effective index n_{eff} is equal in the pump and third-harmonic bands, one typically uses the fundamental mode (e.g., TE11) at the pump wavelength and a higher-order mode for the third-harmonic signal, with odd numbers in both x and y (e.g., TE51 or TE13) often used [14, 16, 19]. Empirically, these are two of the first three rectangular modes that might work, as the other mode (TE31) is typically able to phase-match SHG but not THG [14, 16, 17]. We verify this general behavior in Fig. 2(d), displaying the calculated n_{eff} of the TE51 (blue), c03 | r42 (red), and TE13 (purple) modes at 520 nm, the TE31 mode (dashed green) at 780 nm, and the TE11 mode (black) at 1560 nm. Here we fix the H and vary W, and TE13 shows the flattest dispersion as its confinement is mostly in the y direction and therefore not affected much when changing W. TE51 is more sensitive than c03 | r42 by a similar logic, as its confinement critically depends on W. The vertical dashed lines specify the phase-matching geometries for each configuration. In Fig. 2(e), we show the E_x mode profiles for the 520 nm and 1560 nm modes, on the top and bottom, respectively, for the phase-matched THG geometries.

For these phase-matched cases, we further calculate the mode volumes and mode overlap factors, according to the definitions provided in the supplementary material. The mode volumes of these three schemes (specified in the caption) are close to each other (within 3 %). The mode overlap (specified in Fig. 2(e)) is the dominant factor, and the c03 | r42 hybridized mode is better than TE51, but worse than TE13. However, we note that the vertical field distribution for TE13 tends to exhibit poor coupling to the fundamental TE11 mode of an access waveguide, and therefore a more complex coupling design is needed for efficient coupling, e.g., an additional shallow etching step [20, 21].

For each mode combination, we plot the THG number conversion efficiency in the access waveguide, as shown by solid lines in Fig. 3, and based on the equations presented in the Supplementary Material. If the pump is far from depleted, the conversion efficiency can be estimated in a perturbative regime that is only accurate when conversion efficiency is small (dashed lines). In both cases, we assume all modes are critically coupled, and have loaded Qs of 1×10^6. The hybridized regime requires 3.5× the pump power as TE13 for the same conversion efficiency (assuming all other parameters are the same) due to its weaker modal overlap, but is less challenging in aforementioned microring-waveguide coupling design. It also out-performs the TE51 design due to its better mode overlap, while having similar waveguide coupling characteristics.

In summary, we investigate the hybridization of circular and rectangular mode profiles in nanophotonics. At a visible wavelength, such hybridized modes appear in waveguides that are sufficiently thick to support multi-mode operation, when the aspect ratio remains rectangular (width:thickness = 2:1 in this work). More circular cross-sectional geometries [19, 22] are likely to support such modes better, that is, with stronger hybridization or even pure circular modes. We further show that these hybridized modes can be advantageous in nonlinear optical processes, taking third harmonic generation in a silicon nitride microring resonator as an example. We anticipate that hybridized circular modes will be of particular relevance to wide-band nonlinear processes connected to visible wavelengths, where nanophotonic devices are naturally multi-modal.

Funding. Defense Advanced Research Projects Agency (DARPA-LUMOS); National Institute of Standards and Technology (NIST-on-a-chip).

Acknowledgement. X.L. acknowledges support under the Cooperative Research Agreement between the University of Maryland and NIST-PML.

Disclosures. The authors declare no conflicts of interest.

See Supplement 1 for supporting content.

REFERENCES

1. G. Agrawal, *Fiber-optic communication systems (4th edition)* (Wiley, New Jersey, 2010).
2. G. Agrawal, *Lightwave technology: components and devices* (Wiley, New Jersey, 2004).
3. Y. Wu and K. S. Chiang, Opt. Express **24**, 30108 (2016).
4. K. Saitoh, N. Hanzawa, T. Sakamoto, T. Fujisawa, Y. Yamashita, T. Matsui, K. Tsujikawa, and K. Nakajima, Opt. Fiber Technol. **35**, 80 (2017).
5. G. I. Stegeman and R. H. Stolen, J. Opt. Soc. Am. B **6**, 652 (1989).
6. Q. Lin, O. J. Painter, and G. P. Agrawal, Opt. Express **15**, 16604 (2007).
7. D. J. Moss, R. Morandotti, A. L. Gaeta, and M. Lipson, Nat. Photon. **7**, 597 (2013).
8. A. L. Gaeta, M. Lipson, and T. J. Kippenberg, Nat. Photonics **13**, 158 (2019).
9. Q. Li, M. Davanço, and K. Srinivasan, Nat. Photon. **10**, 406 (2016).
10. X. Lu, G. Moille, Q. Li, D. A. Westly, A. Rao, S.-P. Yu, T. C. Briles, S. B. Papp, and K. Srinivasan, Nat. Photon. **13**, 593 (2019).
11. X. Lu, G. Moille, A. Singh, Q. Li, D. A. Westly, A. Rao, S.-P. Yu, T. C. Briles, S. B. Papp, and K. Srinivasan, Optica **6**, 1535 (2019).
12. A. R. Johnson, A. S. Mayer, A. Klenner, K. Luke, E. S. Lamb, M. R. E. Lamont, C. Joshi, Y. Okawachi, F. W. Wise, M. Lipson, U. Keller, and A. L. Gaeta, Opt. Lett. **40**, 5117 (2015).
13. D. R. Carlson, D. D. Hickstein, A. Lind, S. Droste, D. Westly, N. Nader, I. Coddington, N. R. Newbury, K. Srinivasan, S. A. Diddams, and S. B. Papp, Opt. Lett. **42**, 2314 (2017).
14. J. S. Levy, M. A. Foster, A. L. Gaeta, and M. Lipson, Opt. Express **19**, 11415 (2011).
15. T. Ning, H. Pietarinen, O. Hyvärinen, R. Kumar, T. Kaplas, M. Kauranen, and G. Genty, Opt. Lett. **37**, 4269 (2012).
16. J. B. Surya, X. Guo, C.-L. Zou, and H. X. Tang, Optica **5**, 103 (2018).
17. X. Lu, G. Moille, A. Rao, D. A. Westly, and K. Srinivasan, Nat. Photon. **15**, 131 (2021).
18. G. Moille, Q. Li, T. C. Briles, S.-P. Yu, T. Drake, X. Lu, A. Rao, D. Westly, S. B. Papp, and K. Srinivasan, Opt. Lett. **44**, 4737 (2019).
19. T. Carmon and K. Vahala, Nat. Phys. **3**, 430 (2007).
20. W. C. Jiang, J. Zhang, and Q. Lin, Opt. Express **22**, 1187 (2014).
21. X. Lu, G. Moille, A. Rao, and K. Srinivasan, Opt. Lett. **46**, 222 (2021).
22. M.-C. Lee and M. Wu, J. Microelectromech. Syst. **15**, 338 (2006).

FULL REFERENCES

1. G. Agrawal, *Fiber-optic communication systems (4th edition)* (Wiley, New Jersey, 2010).
2. G. Agrawal, *Lightwave technology: components and devices* (Wiley, New Jersey, 2004).
3. Y. Wu and K. S. Chiang, "Mode-selective coupling between few-mode fibers and buried channel waveguides," Opt. Express **24**, 30108–30123 (2016).
4. K. Saitoh, N. Hanzawa, T. Sakamoto, T. Fujisawa, Y. Yamashita, T. Matsui, K. Tsujikawa, and K. Nakajima, "PLC-based mode multi/demultiplexers for mode division multiplexing," Opt. Fiber Technol. **35**, 80–92 (2017).
5. G. I. Stegeman and R. H. Stolen, "Waveguides and fibers for nonlinear optics," J. Opt. Soc. Am. B **6**, 652–662 (1989).
6. Q. Lin, O. J. Painter, and G. P. Agrawal, "Nonlinear optical phenomena in silicon waveguides: Modeling and applications," Opt. Express **15**, 16604–16644 (2007).
7. D. J. Moss, R. Morandotti, A. L. Gaeta, and M. Lipson, "New cmos-compatible platforms based on silicon nitride and hydex for nonlinear optics," Nat. Photon. **7**, 597–607 (2013).
8. A. L. Gaeta, M. Lipson, and T. J. Kippenberg, "Photonic-chip-based frequency combs," Nat. Photonics **13**, 158–169 (2019).
9. Q. Li, M. Davanço, and K. Srinivasan, "Efficient and low-noise single-photon-level frequency conversion interfaces using silicon nanophotonics," Nat. Photon. **10**, 406–414 (2016).
10. X. Lu, G. Moille, Q. Li, D. A. Westly, A. Rao, S.-P. Yu, T. C. Briles, S. B. Papp, and K. Srinivasan, "Efficient telecom-to-visible spectral translation using silicon nanophotonics," Nat. Photon. **13**, 593–601 (2019).
11. X. Lu, G. Moille, A. Singh, Q. Li, D. A. Westly, A. Rao, S.-P. Yu, T. C. Briles, S. B. Papp, and K. Srinivasan, "Milliwatt-threshold visible–telecom optical parametric oscillation using silicon nanophotonics," Optica **6**, 1535–1541 (2019).
12. A. R. Johnson, A. S. Mayer, A. Klenner, K. Luke, E. S. Lamb, M. R. E. Lamont, C. Joshi, Y. Okawachi, F. W. Wise, M. Lipson, U. Keller, and A. L. Gaeta, "Octave-spanning coherent supercontinuum generation in a silicon nitride waveguide," Opt. Lett. **40**, 5117–5120 (2015).
13. D. R. Carlson, D. D. Hickstein, A. Lind, S. Droste, D. Westly, N. Nader, I. Coddington, N. R. Newbury, K. Srinivasan, S. A. Diddams, and S. B. Papp, "Self-referenced frequency combs using high-efficiency silicon-nitride waveguides," Opt. Lett. **42**, 2314–2317 (2017).
14. J. S. Levy, M. A. Foster, A. L. Gaeta, and M. Lipson, "Harmonic generation in silicon nitride ring resonators," Opt. Express **19**, 11415–11421 (2011).
15. T. Ning, H. Pietarinen, O. Hyvärinen, R. Kumar, T. Kaplas, M. Kauranen, and G. Genty, "Efficient second-harmonic generation in silicon nitride resonant waveguide gratings," Opt. Lett. **37**, 4269–4271 (2012).
16. J. B. Surya, X. Guo, C.-L. Zou, and H. X. Tang, "Efficient third-harmonic generation in composite aluminum nitride/silicon nitride microrings," Optica **5**, 103–108 (2018).
17. X. Lu, G. Moille, A. Rao, D. A. Westly, and K. Srinivasan, "Efficient photo-induced second harmonic generation in silicon nitride photonics," Nat. Photon. **15**, 131–136 (2021).
18. G. Moille, Q. Li, T. C. Briles, S.-P. Yu, T. Drake, X. Lu, A. Rao, D. Westly, S. B. Papp, and K. Srinivasan, "Broadband resonator-waveguide coupling for efficient extraction of octave-spanning microcombs," Opt. Lett. **44**, 4737–4740 (2019).
19. T. Carmon and K. Vahala, "Visible continuous emission from a silica microphotonic device by third-harmonic generation," Nat. Phys. **3**, 430–435 (2007).
20. W. C. Jiang, J. Zhang, and Q. Lin, "Compact suspended silicon microring resonators with ultrahigh quality," Opt. Express **22**, 1187–1192 (2014).
21. X. Lu, G. Moille, A. Rao, and K. Srinivasan, "Proposal for noise-free visible-telecom quantum frequency conversion through third-order sum and difference frequency generation," Opt. Lett. **46**, 222–225 (2021).
22. M.-C. Lee and M. Wu, "Thermal annealing in hydrogen for 3-D profile transformation on silicon-on-insulator and sidewall roughness reduction," J. Microelectromech. Syst. **15**, 338–343 (2006).